Astron. Astrophys. 334, 124–138 (1998)

ASTRONOMY
AND
ASTROPHYSICS

Spectroscopy of the circumnuclear emission line regions in Seyfert galaxies*

II. NGC 7214

Mario Radovich, Piero Rafanelli, and Roberto Barbon

Department of Astronomy, University of Padova, Vicolo dell'Osservatorio 5, I-35122 Padova, Italy

Received 19 March 1997 / Accepted 17 December 1997

Abstract. This paper is the second of a series (Radovich and Rafanelli 1996) devoted to the investigation of the emission line properties of the circumnuclear and extranuclear regions in a sample of nearby Seyfert galaxies. Our aim is to identify star formation regions around the active nucleus and to derive their properties like star formation rate and dust content, and compare them with those observed in non-active galaxies.

We show that photoionization models may fit the observed line ratios both in the nuclear and circumnuclear regions of the Sy 1.2 galaxy NGC 7214. In the nucleus, components with different densities must be considered. In the circumnuclear regions, line ratios to projected distances of $\sim$ 2 kpc from the nucleus are typical of ionization by a power law. At higher distances ($\sim$ 5–8 kpc) they are fitted either by a thermal continuum or assuming that both stars and the non thermal source contribute to the ionization of the gas. A simple interpretation is suggested, in the framework of the unified model for Seyfert galaxies. Evidence for enhanced star formation, maybe related to the ongoing interaction with a close spiral galaxy, is found in only one region.

Key words: galaxies: Seyfert – galaxies: individual: NGC 7214

1. Introduction

There is growing evidence that a link exists between Seyfert activity and interaction. Numerical simulations (Barnes and Hernquist 1992, Hernquist and Mihos 1995) show that nuclear activity may be triggered by mergers; Rafanelli et al. (1995) found an excess of interacting pairs among Seyfert galaxies.

Closely related to this topic is that of the circumnuclear environment in Seyfert galaxies. If nuclear activity is triggered by interaction with a companion galaxy via the transport of gas from the disk to the nucleus, it is very likely that bursts of star formation are also produced during the gas inflow. In this case we expect the existence of a relationship between the properties of the circumnuclear environment (dust amount, star formation) and the evolutionary stage of the AGN.

Indeed, many observations suggest that circumnuclear star formation is more frequent in Seyfert 2's than Seyfert 1's (see Moorwood 1996). This may indicate that Seyfert 2's are in an earlier evolutionary stage than Seyfert 1's, whereas in the so-called unified model (Antonucci 1993) this dichotomy is simply explained with the orientation of an obscuring torus to the line of sight. It is therefore of primary importance to collect as many data as possible about the physical conditions around the nuclei of Seyfert 1 and Seyfert 2 galaxies, in order to have a reasonable large amount of data to test the above predictions.

NGC 7214(= VV 700, z=0.023, $m_{\rm B} = 12.48$) was classified as a Seyfert 1.2 by Dahari (1985) and Winkler (1992); its morphological type is SB(s)bc according to de Vaucouleurs et al. (1991). The galaxy is one (A) of the four components of the Hickson group H91 (Hickson 1982), is closely interacting with the companion SBa galaxy H91D, which is located at 0.6′N, and it shows a strongly disturbed morphology (see Fig. 1): evidence of interaction between NGC 7214 and H91C is given by the existence of faint distorted spiral arms stretching out between the two galaxies. Interaction is likely to induce bursts of star formation in HII regions surrounding the Seyfert nucleus and to power the far infrared emission, $L_{60-100\mu m} = 1.33 \times 10^{44}\,{\rm erg\,s^{-1}}$ (Lonsdale 1989). This would also explain the relatively high emission at 60μm compared to that at 25μm, which corresponds to $\alpha(60,25) = -2.00$ steeper than in a typical Sy1, where $\alpha(60,25) > -1.5$ (see Fig. 4 of Mulchaey et al. 1994).

In this paper we use long-slit spectroscopy and Hα narrow-band imaging in order to study the physical properties (nature of ionization source, gas density and ionization parameter) and the kinematics of the nuclear and circumnuclear regions of the galaxy. In particular, our aim is to understand whether the main ionization source at different projected distances from the nucleus is non-thermal (AGN) or thermal (HII regions).

In Sect. 2 we describe the observations and their reduction. In Sect. 3 we discuss the observed emission line ratios, the velocity curve and the data derived from Hα narrow-band imaging. The interpretation of the line ratios is discussed in Sect. 4, where we discriminate thermal and non-thermal ionized regions. For

---

Send offprint requests to: P. Rafanelli

* Based on observations collected at ESO - La Silla (Chile)

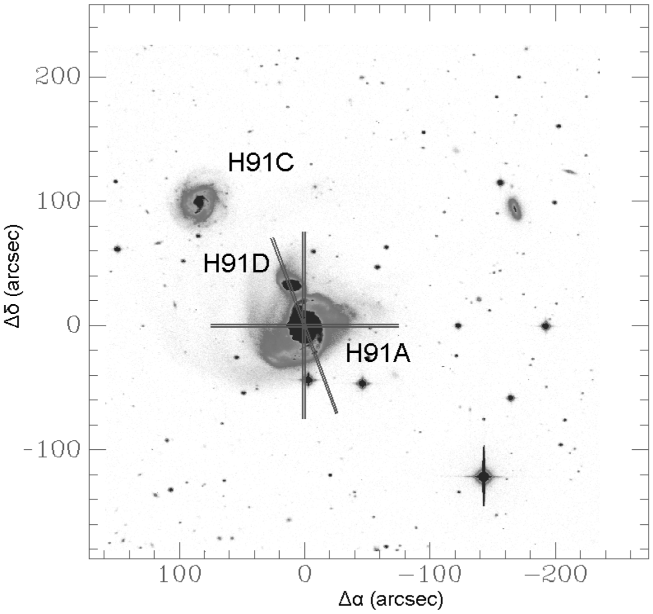

Fig. 1. The H91 field imaged through the R filter with EFOSC2 at the 2.2m. The positions of the slit (P.A.=180°, 200°, 270°) are overlaid. North is at the top, east at the left.

those regions where the ionization has been shown to be in prevalence thermal, we compute the star formation rates: these are compared with the values given in literature for normal spiral galaxies (Kennicutt 1988).

2. Observations and reductions

Long-slit spectra of NGC 7214 have been obtained at ESO La Silla (Chile) at the 3.6m with the Eso Faint Object Spectrograph and Camera (EFOSC). The spectra were taken on June 8–11, 1994 at position angles P.A. = 180°, 200° and 270° using the B150 and O150 grisms for each position of the slit which was $2''$ wide both nights; the seeing was $\sim 3''$. The log of the observations is given in Table 1. All spectra were taken when the object was at a zenith distance $< 35°$. The loss of light due to the differential atmospheric refraction was therefore low even if the slit was not exactly located along the parallactic angle. The uncertainty in the flux calibration, as derived from the observation of standard photometric stars, is $\leq$ 20%.

The spectral resolution is 10Å at 5700 Å, as measured from the FWHM of a faint comparison line. In all cases, the standard reduction steps have been applied to the the two–dimensional spectra: they have been bias subtracted, divided by flat field, wavelength calibrated, corrected for atmospheric extinction and then transformed in energy flux units and sky subtracted using the LONGSLIT and DEREDDEN tasks in the NOAO's imaging analysis software IRAF. The Galactic extinction is very low, A_B = 0.01 mag (Burstein and Heiles 1984), and no correction for it was applied.

Three images were taken on November 1996 in R ($\lambda_c = 6439$Å, FWHM = 1675Å), redshifted Hα ($\lambda_c = 6729$Å, FWHM = 64Å) and continuum ($\lambda_c = 6559$Å, FWHM = 14Å) at the ESO 2.2m telescope with EFOSC2; the seeing during this night was $\sim 1.2''$. All the images have been bias subtracted, divided for the flat field, cleaned from cosmic rays and background subtracted. The Hα and continuum images have been calibrated in flux observing a standard star and taking into account the different transmission profiles of the two filters; the flux calibrated images were corrected for atmospheric extinction and a constant background measured in emission-free regions was subtracted. The continuum image was aligned to the Hα image using field stars close to the galaxy and then subtracted from it; a check that the scaling factor derived from the photometric calibration was correct was given by the disappearance of non saturated stars in the continuum-subtracted image. We estimated the uncertainty in the flux calibration to be $\sim$ 30%. The contour map of the continuum subtracted Hα image of NGC 7214 is shown in Fig. 2; the R image of the H91 field is shown in Fig. 1.

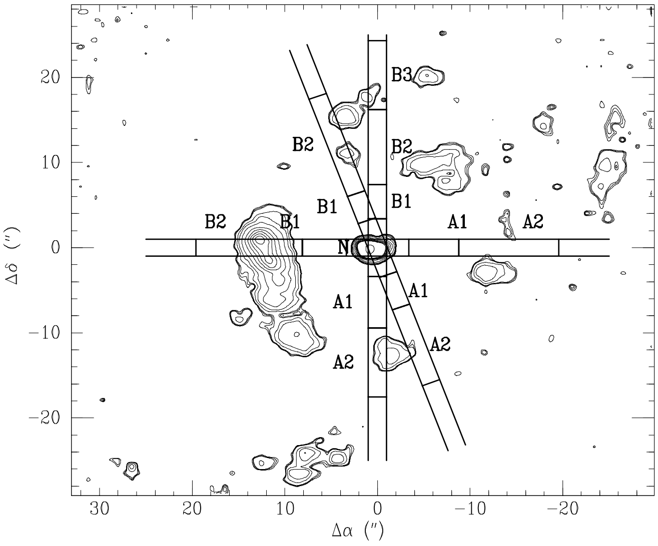

Fig. 2. Contour map of the continuum subtracted Hα image of NGC 7214.

The linear scale is 0.45 kpc/$''$ (z=0.023, H_0 = 75 km s^{-1} Mpc^{-1}).

3. Results

3.1. Emission line regions

Different emitting regions were extracted from the two-dimensional spectra on the basis of the size of extended emission features of the Hα and [NII] lines. These regions are illustrated in the contour map of the continuum subtracted Hα+[NII] image (Fig. 2); angular and projected linear sizes and the central distances from the nucleus of each region are given in Table 2. In order to simplify the discussion of the properties of different regions at different position angles, these will be indicated with a subscript (e.g. $A2_{270}$). The atmospheric bands have been removed dividing each one-dimensional spectrum by the normalized spectrum of a flux standard star. 1D spectra for different position angles are shown in Fig. 3, 4 and 5.

Table 1. Log of the observations

Date	P.A.	grism	slit aperture	exposure	zenith angle	parallactic angle
8 Jun 94	270	B150	2″	1800 s	27°	80°
8 Jun 94	270	O150	2″	1800 s	18°	81°
8 Jun 94	200	B150	2″	1800 s	2°	128°
8 Jun 94	200	O150	2″	2700 s	9°	78°
11 Jun 94	180	B150	2″	1200 s	26°	80°
11 Jun 94	180	O150	2″	1200 s	32°	79°

B150: $\lambda\lambda$3740-5450 Å
O150: $\lambda\lambda$5160-6930 Å

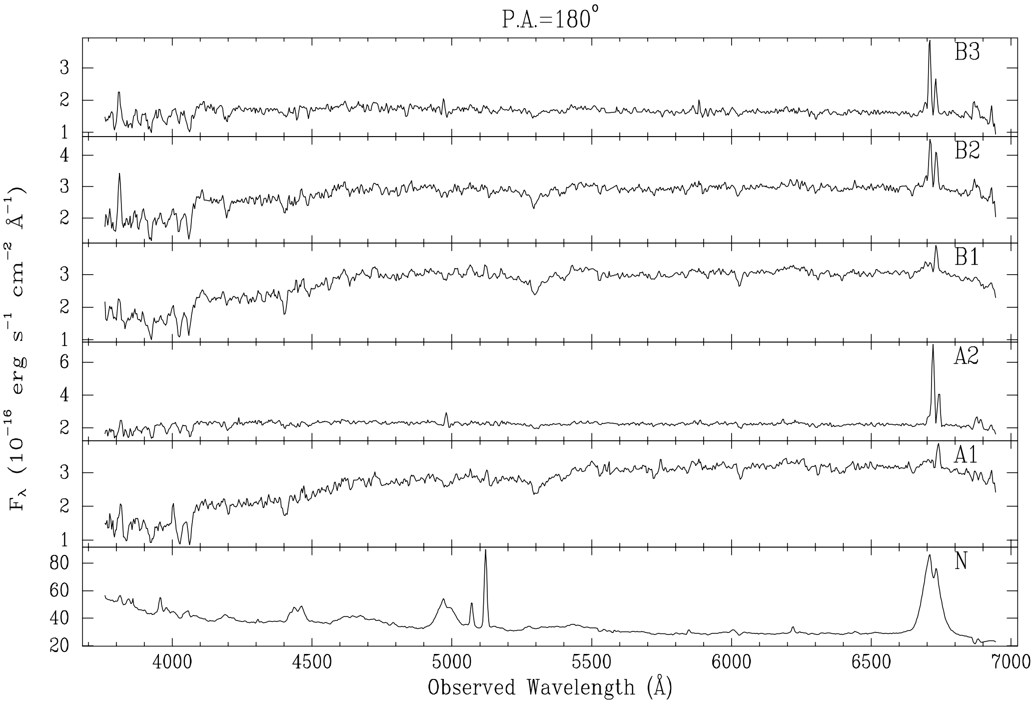

Fig. 3. Concatenated observed blue and red spectra, P.A.=180°

It is evident from the analysis of the 1D spectra that the underlying stellar absorption must be removed in order to measure the line fluxes, in particular in the inner circumnuclear regions (A1 and B1 regions). To this aim we used as a template the integrated spectrum of the companion galaxy H91D, obtained at P.A. = 200°, which is free of emission lines and has a good signal to noise ratio. This has the advantage that both the spectra to be corrected and the template one have been taken in the same instrumental and atmospheric conditions. For each spectrum we followed the procedure described by Ho et al. (1993), namely:

- We first removed the redshifts by the wavelength determination of several absorption lines.
- The ratio of the object spectrum to the template spectrum was fitted by a cubic spline in order to determine a wavelength-dependent scaling factor.
- The template spectrum was multiplied by the resulting curve and subtracted from the object spectrum.

In the case that the subtraction of the template spectrum did not give satisfactory results, that is when the equivalent width of the absorption lines in the two spectra were not the same, we added to the template an offset in order to dilute the absorption lines and started again the procedure, until a reasonable result was achieved. Due to the weakness of the absorption lines, no template correction was applied to the spectra in the nuclear regions; the correction was however applied to the spectra of all circumnuclear regions (A_n, B_n, n=1–3).

In the circumnuclear regions, line positions and fluxes were measured using the SPLOT task in IRAF. The [NII] satellites of Hα and the components of the [SII] doublet were deblended using a multiple gaussian fit and then measured. The gaussian approximation is justified by the shape of the line profiles as obtained with our resolution. The deblending procedure available in SPLOT failed when we tried to deblend the broad and narrow components of the permitted lines in the nuclear regions. We then used a procedure which allows to choose whether the fitting parameters such as the line width and position should be fixed to a given value or varied to give the best solution. We first fitted the continuum by a spline and subtracted it, and then made the deblending: a detailed discussion of the procedures followed in the deblending of the line components in the nucleus is given in Sect. 3.1.1. The measured line fluxes relative

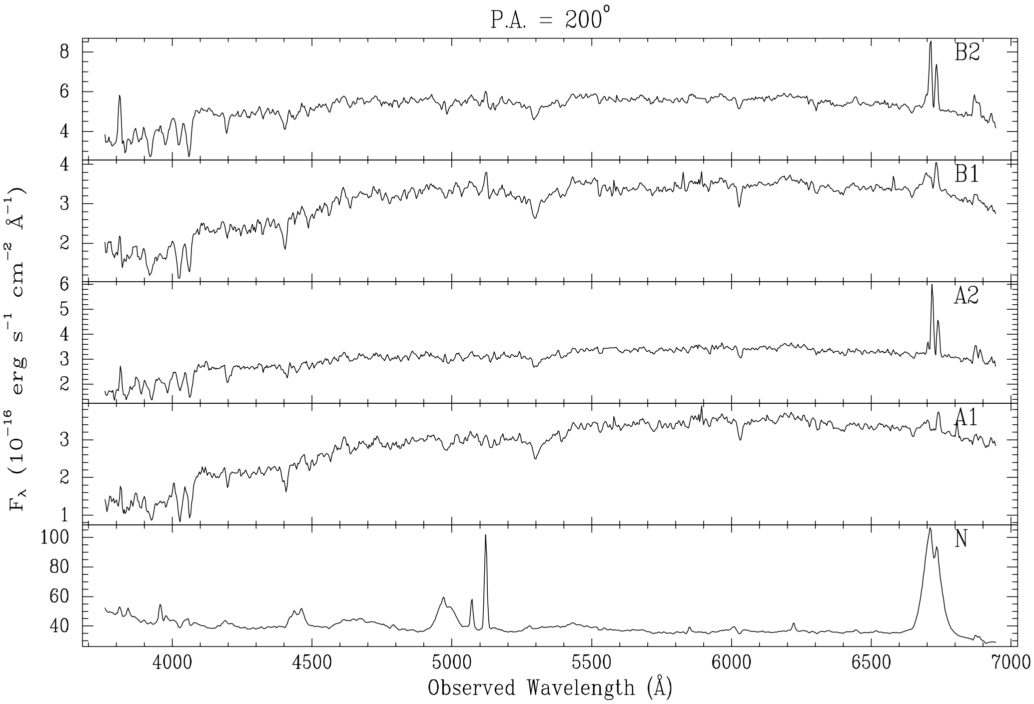

Fig. 4. Concatenated observed blue and red spectra, P.A.=200°

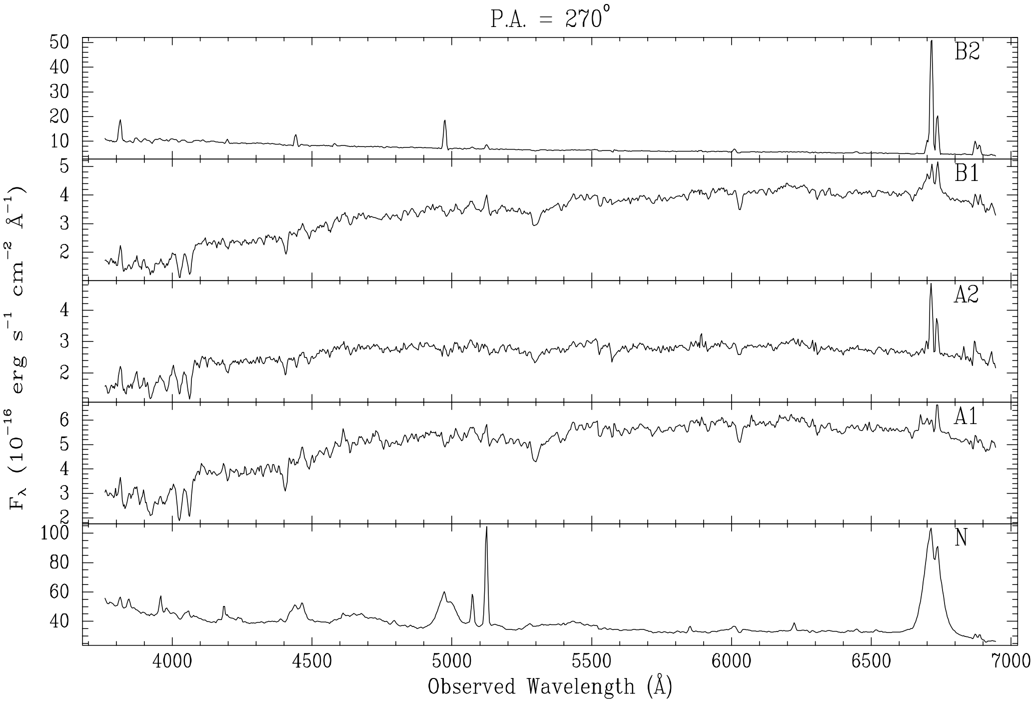

Fig. 5. Concatenated observed blue and red spectra, P.A.=270°

to Hβ are shown in Table 3 (nucleus), in Table 4 (inner circumnuclear regions A1 and B1) and in Table 5 (outer circumnuclear regions A2, B2, B3); dots indicate that the line was not detected in the spectrum. Also shown are the uncertainties due to the choice of the continuum level: they were estimated from the ratio between the amplitude of the line and the standard deviation from the average continuum in an adjacent window devoid of emission lines.

The procedure followed in the analysis of the line ratios is the same described in Radovich and Rafanelli (1996): for each of the emission line regions we used, when possible, the diagnostic line ratios (Veilleux and Osterbrock 1987, hereafter VO) [OI] λ6300/Hα, [SII] λ6724/Hα[1] and [NII] λ6583/Hα vs. [OIII] λ5007/Hβ in order to verify whether the source of the ionization is thermal (HII regions) or not (AGN-like).

---

[1] We indicate as [SII] λ6724 the sum of the [SII] $\lambda\lambda$6716,6731 lines.

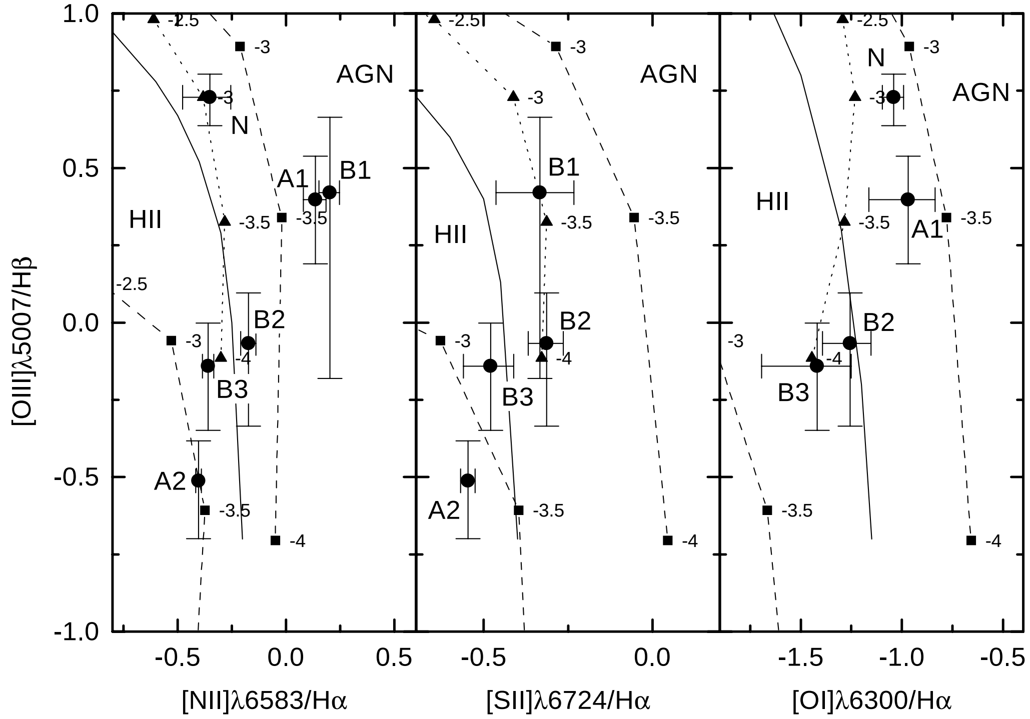

Fig. 6. Diagnostic line ratios observed at P.A.=180°; the solid lines divide AGNs from HII regions (Veilleux and Osterbrock 1987); line ratios in the nucleus (N) are those from the narrow component only. Squares show results from single component photoionization model computed for different values of the ionization parameters. Non thermal models: $\alpha = -1.5$, $n_{\rm H} = 10^3\,{\rm cm}^{-3}$; Thermal models: $T_* = 38\,000$ K, $n_{\rm H} = 10^2\,{\rm cm}^{-3}$. Triangles give the results of composite models computed with $n_{\rm H} = 10^2\,{\rm cm}^{-3}$, a thermal component with $T_* = 38\,000$ K and $\log U_{\rm th} = -3.5$ plus a non thermal component, power-law with $\alpha = -1.5$ and $\log U_{\rm pl}$ varying from -4.0 to -2.0.

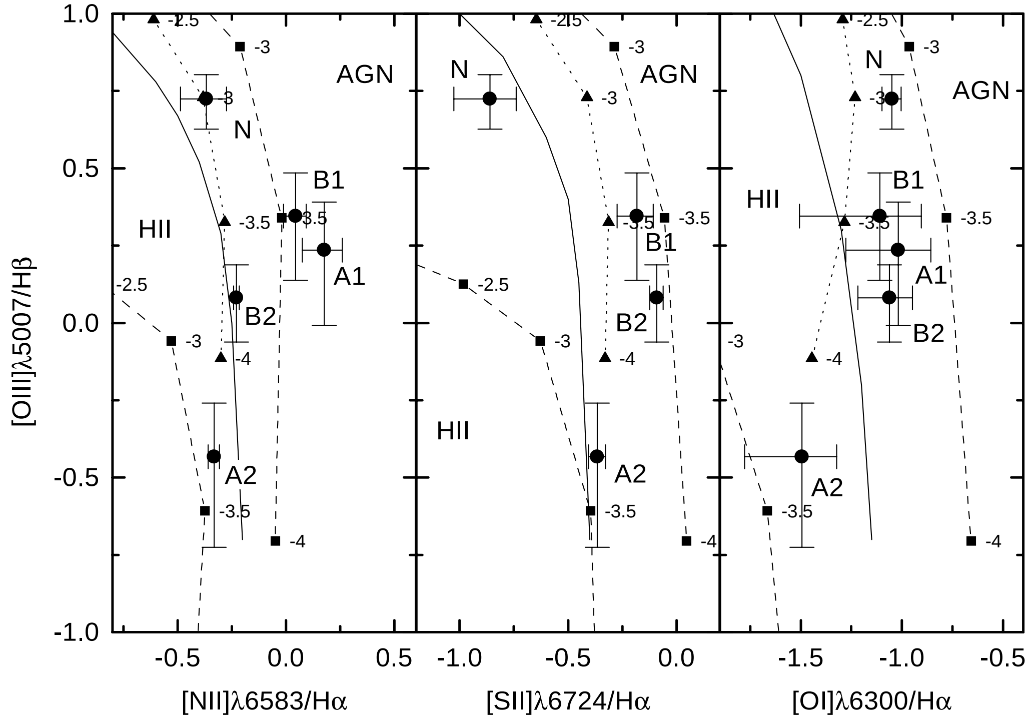

Fig. 7. Diagnostic line ratios observed at P.A.=200°. Symbols are defined as before.

We then tried to fit the observed line ratios with photoionization models computed using the latest release of Gary Ferland's code Cloudy 90 (Ferland 1997): the results are shown in Table 6. In order to simplify the comparison between observed and model line ratios, we plotted for the nucleus and one of the circumnuclear regions in Fig. 12 a 'synthetic' spectrum where the line fluxes given as output by the models have been convolved with a gaussian profile and plotted over a constant-level continuum (F_λ = cost). We assumed gaussian profiles with a constant FWHM and scaled the continuum level to reproduce the observed Hβ equivalent width.

3.1.1. Nucleus

The nuclear spectrum of NGC 7214 is typical of 'intermediate' (1.2 and 1.5) Seyfert galaxies: narrow components are clearly

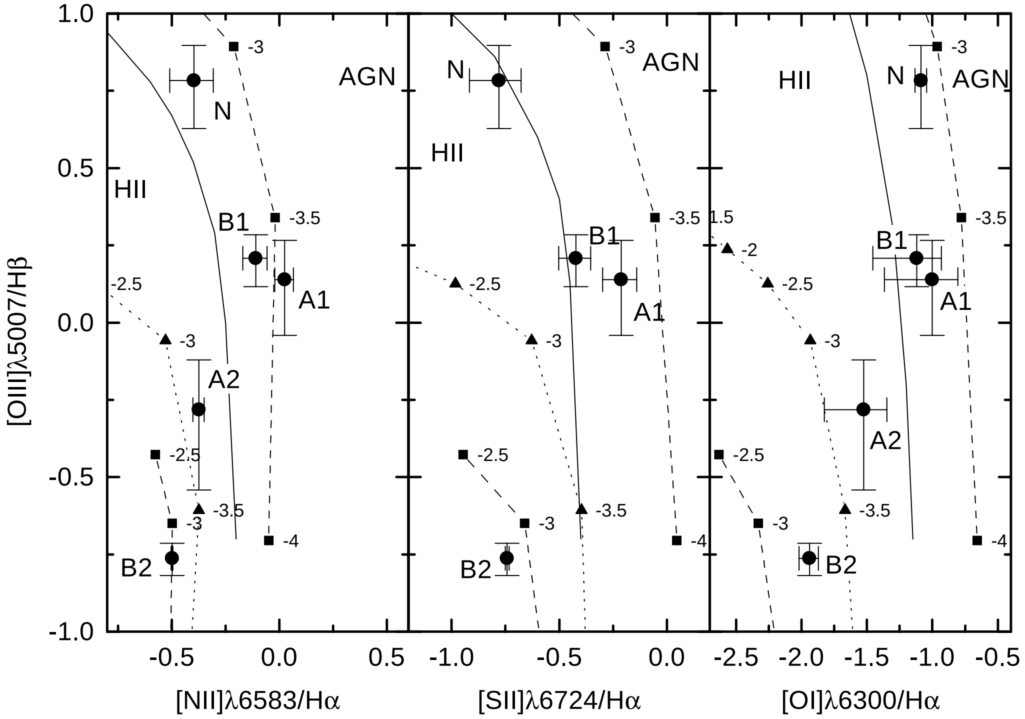

Fig. 8. Diagnostic line ratios observed at P.A.=270°. Parameters for non-thermal models are the same as before, in the HII region side the parameters are: $T_* = 38\,000$ K, $n_{\rm H} = 10^2\,{\rm cm}^{-3}$ (triangles); $T_* = 35\,000$ K, $n_{\rm H} = 10^2\,{\rm cm}^{-3}$ (squares).

Table 2. Size, distance from the nucleus and position angle of the emitting regions in NGC 7214

Region	size		distance		P.A.
	$''$	kpc	$''$	kpc	°
Extranuclear regions					
A2	8.10	3.61	−13.50	−6.02	180
B2	8.78	3.91	11.81	5.27	180
B3	8.10	3.61	20.25	9.03	180
A2	9.45	4.21	−12.15	−5.42	200
B2	12.15	5.42	12.83	5.72	200
A2	10.80	4.81	−14.18	−6.32	270
B2	11.48	5.11	13.84	6.17	270
Circumnuclear regions					
A1	6.08	2.71	−6.41	−2.86	180
B1	4.05	1.81	5.40	2.41	180
A1	4.05	1.81	−5.40	−2.41	200
B1	3.38	1.50	5.06	2.26	200
A1	5.40	2.41	−6.08	−2.71	270
B1	4.73	2.11	5.74	2.56	270
Nucleus					
N	6.75	3.01	0.00	0.00	
Others					
H91D	6.75	3.01	37.80	16.85	20

visible superposed on broad permitted emission lines, with line widths similar to those of forbidden lines (Osterbrock and Koski 1976, Cohen 1983).

The analysis of the profiles of Balmer lines reveals the presence of at least three components (Fig. 9): the deblending of the lines was therefore done with three gaussians. The FWHM of the first component (11Å, ~ 300 km s^{-1} after the correction for the instrumental resolution) was set to the value measured in [OIII] $\lambda5007$; the FWHM of the other two components resulted to be ~ 12Å and ~ 70Å, giving velocity dispersions after the correction for the instrumental resolution of ~ 400 km s^{-1} and ~ 4000 km s^{-1} respectively. Since we are not sure about the physical reliability of the deblending of the narrow components (NL1 and NL2) of the Balmer lines, the fluxes measured in these components were summed together in order to make a comparison with the fluxes measured in the forbidden lines, where such deblending was not possible. The deblending of the Hβ+[OIII] complex was complicated by the presence of residuals in the blue and red wings of the [OIII] lines, which we identified as the $\lambda\lambda$4924, 5018 lines of FeII. Uncertainties on fluxes given by the procedure were in the order of 10%.

A common feature in intermediate Seyfert galaxies is the presence of strong high ionization lines such as [FeVII] λ3759, [FeVII] λ5721, [FeVII] λ6087 and [FeX] λ6375. Cohen (1983) gave for a sample of 14 intermediate Seyferts: [FeVII] λ6087/Hβ $= 0.17 \pm 0.19$, [FeX] λ6375/Hβ $= 0.11 \pm 0.13$; the values measured in NGC 7214 are ~ 0.5 and 0.2 respectively. High ionization lines may arise either from a high density ($n_{\rm e} \sim 10^7\,{\rm cm}^{-3}$) gas located between the BLR and the NLR (Osterbrock 1981) or from highly ionized low-density gas ($n_{\rm e} < 10\,{\rm cm}^{-3}$) located outside the NLR (Korista and Ferland 1989, see also Ferguson et al. 1997 for a more recent discussion on coronal lines in Seyfert galaxies). As concerns the iron lines, the first possibility is more likely, given the well known correlation existing in many Seyfert galaxies between the ionization potential and critical density of these lines and their width (De Robertis and Osterbrock 1984). This correlation is

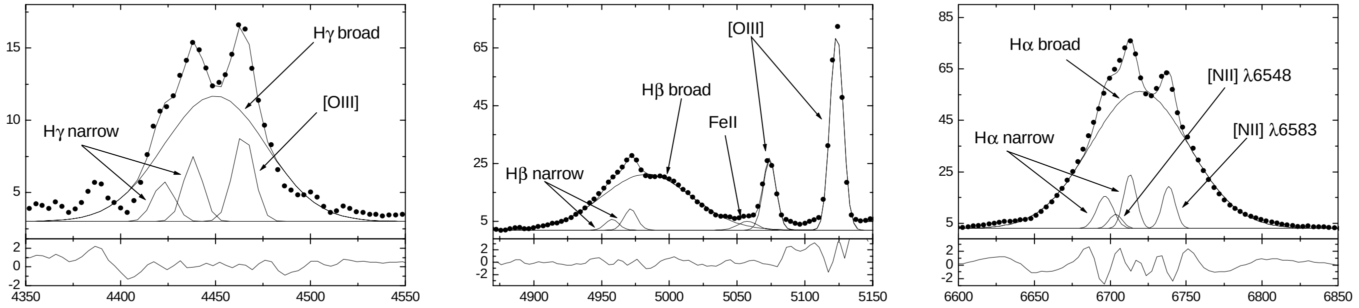

Fig. 9. Deblended broad and narrow components in Hγ + [OIII] λ4363, Hβ + [OIII] $\lambda\lambda$4959,5007 and Hα + [NII] λ6583. The profiles at P.A.=270° are shown here, the same results have been obtained at the other position angles.

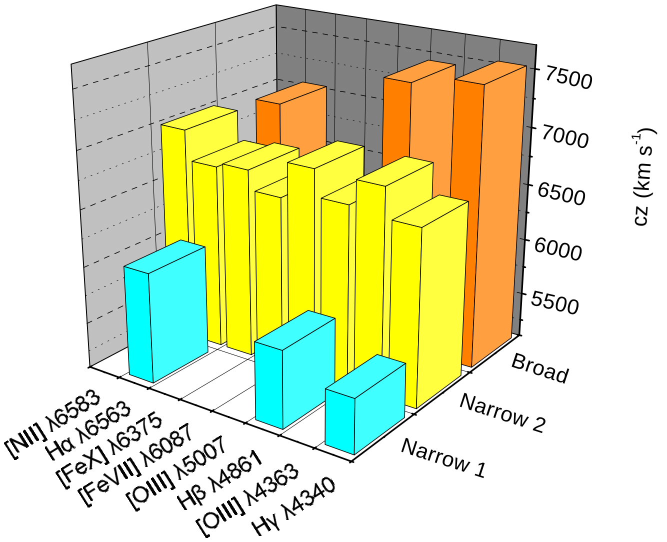

Fig. 10. Centroid line velocities for different emission lines in the nuclear spectra, computed from the average of the values measured at each position angle.

not apparently present in our spectra, but this point should be investigated with higher spectral resolutions than ours.

A strong [OIII] λ4363 is also present: assuming a density $n_{\rm H} \sim 10^3 - 10^4\,{\rm cm}^{-3}$, the ratio [OIII] λ4363/[OIII] $\lambda\lambda(4959+5007) \sim 0.1$ would imply an implausibly high electron temperature, $T_{\rm e} > 7 \times 10^4$ K. This again suggests that we see a component whose gas density is close to 10^7 cm^{-3}.

In addition to strong high-ionization iron lines, emission lines from FeII multiplets centered at 4570 Å, 4924 Å, 5018 Å and 5169 Å (Joly 1988) are also present.

The velocity distribution of narrow and broad lines is shown in Fig. 10. Narrow lines are blueshifted ($cz \sim 6800\,{\rm km\,s}^{-1}$) compared to broad lines ($cz \sim 7300\,{\rm km\,s}^{-1}$); the third component in the Balmer lines is even more blueshifted, $cz \sim 5800\,{\rm km\,s}^{-1}$.

The estimate of internal dust extinction from the Hα/Hβ ratio is difficult since at high densities collisional effects become important and the Case B assumption is no more valid (Osterbrock 1989); in addition, the deblending of the broad and narrow component is uncertain. We temptatively adopted for narrow lines the value derived from the photoionization models computed in Sect. 4, which results to be the same as the Case B value, Hα/Hβ = 2.80: the derived values of E(B–V) are low, E(B–V) $\sim 0 - 0.1$. No extinction was applied for the broad lines, since the 'true' Hα/Hβ is unknown and can't be reliably determined by photoionization models. The line ratios measured summing together broad and narrow components are in good agreement with the values given for NGC 7214 by Dahari (1985) and Winkler (1992).

Table 3. Observed broad (*b*) and narrow (*n*) nuclear line ratios and fluxes in units of 10^{-14} erg s^{-1} cm^{-2}. A colon indicates ratios where deblending was particularly uncertain.

		P.A. = 180°		P.A. = 200°		P.A. = 270°	
Line	λ	b	n	b	n	b	n
[OII]	3727	...	0.57	...	0.42	...	0.58
[FeVII]	3759	...	0.46	...	0.42	...	0.52
[NeIII]	3869	...	1.02:	...	1.19:	...	0.96:
H8	3888	0.19	0.18	0.18	0.23	0.20	0.15
[NeIII]+Hϵ	3968,3970	0.85		0.92		0.93	
Hδ	4102	0.14	0.19	0.16	0.22	0.17	0.51
Hγ	4340	0.44	0.69	0.43	0.65	0.37	0.71
[OIII]	4363	...	0.58	...	0.56	...	0.62
HeII	4686	...	0.29:	...	0.33:	...	0.32:
Hβ	4861	1.00	1.00	1.00	1.00	1.00	1.00
[OIII]	4959	...	1.95	...	1.88	...	2.17
[OIII]	5007	...	5.37	...	5.29	...	6.05
[FeVII]	5721	...	0.37	...	0.39	...	0.37
HeI	5876	0.15	0.17	0.24	0.20	0.17	0.25
[FeVII]	6087	...	0.48	...	0.59	...	0.56
[OI]	6300	...	0.25	...	0.27	...	0.26
[FeX]	6375	...	0.26	...	0.22	...	0.18
Hα	6563	2.75	2.80	3.17	2.99	2.75	3.14
[NII]	6583	...	1.25	...	1.29	...	1.26
[SII]	6716	...	...	...	0.22	...	0.24
[SII]	6724	...	...	...	0.41	...	0.52
[SII]	6731	...	...	...	0.20	...	0.28
F(Hα)		35.2	3.6	43.0	4.3	43.9	4.3
F(Hβ)		12.8	1.3	13.5	1.4	15.9	1.4

3.1.2. Circumnuclear and extranuclear regions

Figs. 6, 7 and 8 show the positions in the VO diagnostic diagrams of the line ratios measured in the circumnuclear regions. The same line ratios are shown in Table 4 and in Table 5.

Line ratios in the inner circumnuclear regions A1 and B1 (projected distance $\sim$ 2 kpc) are typical of power-law ionization: [OIII]/H$\beta \sim 1.4-2.5$, [NII]/H$\alpha \sim 0.8-1.5$, [SII]/H$\alpha \sim 0.4-0.7$, [OI]/H$\alpha \leq 0.1$. Considering the weakness of the Balmer line fluxes and that their determination strongly relies on the template correction procedure, we conclude that they are most likely clouds of gas ionized by the AGN.

In the outer regions we have that [OIII]/H$\beta \sim 0.2-1.2$, [NII]/H$\alpha \sim 0.3-0.7$, [SII]/H$\alpha \sim 0.2-0.8$, [OI]/H$\alpha \sim 0-0.1$: these values are more typical of HII regions, but in some cases they are intermediate between HII and AGN values. More in detail, from the VO diagrams it appears that:

P.A.=180° – The line ratios in A2 and B3 are in agreement with HII region values, [OIII]/H$\beta \sim 0.3$ and 0.7 respectively, [NII]/H$\alpha \sim 0.4$, [OI]/H$\alpha \sim 0.04$ in B3 (it could not be measured in A2), [SII]/H$\alpha \sim 0.3$. In B2 the line ratios are located on the AGN side of the diagram, [NII]/H$\alpha \sim 0.7$, [OI]/H$\alpha \sim 0.06$, [SII]/H$\alpha \sim 0.5$.

P.A.=200° – A2 is most likely an HII region, [OIII]/H$\beta \sim 0.4$, [NII]/H$\alpha \sim 0.5$, [OI]/H$\alpha \sim 0.03$, [SII]/H$\alpha \sim 0.4$. B2 is more AGN-like, [OIII]/H$\beta \sim 1.2$, [NII]/H$\alpha \sim 0.6$, [OI]/H$\alpha \sim 0.09$,[SII]/H$\alpha \sim 0.8$.

P.A.=270° – B2 is a typical low ionization HII region, [OIII]/H$\beta \sim 0.2$, [NII]/H$\alpha \sim 0.3$, [OI]/H$\alpha \sim 0.01$, [SII]/H$\alpha \sim 0.2$. In A2 we have [OIII]/H$\beta \sim 0.5$, [NII]/H$\alpha \sim 0.4$, [OI]/H$\alpha \sim 0.03$ while [SII] lines could not be measured: the ionization source is most likely thermal.

To summarize, the regions named as B2 at P.A.=180° and 200° show ratios which are shifted toward the AGN side of the VO diagram, whereas in the other regions the values are more typical of HII regions.

The amount of extinction derived from the Hα/Hβ ratios is uncertain in the inner regions (A1, B1), where the Balmer lines are almost completely obliterated by the absorption lines of the underlying galaxy and can be measured only after the template subtraction. In the outer regions, we have Hα/H$\beta \sim$ 4–7. Assuming the Case B recombination value (Osterbrock 1989) 2.80 as the intrinsic value of Hα/Hβ, we have that the reddening E(B–V) is in the range $\sim 0-0.4$ in the A1,B1 regions, $\sim$ 0.3–0.9 in the other ones. We used these values in order to correct for internal extinction the observed line fluxes and ratios; the correction for reddening was performed assuming the reddening law of Whitford (1958) as parametrized by Miller and Mathews (1972). The dereddened line ratios are also given in Tables 4,5.

In those cases where a reliable measure of the [SII] $\lambda\lambda$6716/6731 was possible we derived the electron density, which resulted to be $\leq 100\,\mathrm{cm}^{-3}$.

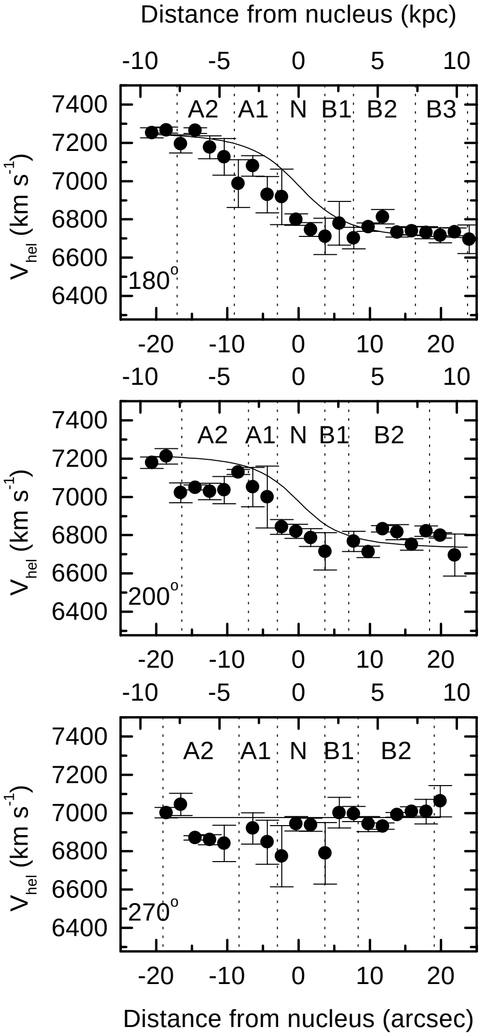

Fig. 11. Heliocentric radial velocities measured from emission lines. The solid line is the velocity curve computed assuming pure circular motions.

3.2. Kinematics

The velocity curve was constructed using the RVIDLINES task in IRAF, which computes at each point along the slit the mean heliocentric radial velocity from the centroids of the emission lines. We selected a binning of 3 pixels along the slit and, when this could be done unambiguously, we measured the centroids of the following emission lines: [OII] λ3727, H$\beta\lambda$4861, [OIII] λ5007, [OI] λ6300, H$\alpha\lambda$6563, [NII] λ6583 and [SII] $\lambda\lambda$6716, 6731.

The velocity curve is flat at P.A. = 270°, which indicates for the nodal line the position angle P.A. = 180°. For comparison only, we tried to fit the observed velocity curves with the law given by Bertola et al. (1991) in the case of circular orbits:

$$V(R,\Psi) = V_{\rm sys} + \qquad (1)$$
$$\frac{aR\cos\left(\Psi-\Psi_0\right)\sin i\cos^p i}{\left\{R^2\left[\sin^2\left(\Psi-\Psi_0\right)+\cos^2 i\cos^2\left(\Psi-\Psi_0\right)\right]+c^2\cos^2 i\right\}^{p/2}},$$

Table 4. Emission line ratios in the circumnuclear regions. Fluxes are given in units of 10^{-16} erg s^{-1} cm^{-2}; fluxes and ratios corrected for extinction are printed in bold.

		P.A. = 180°		P.A. = 200°		P.A. = 270°	
Line	λ	A1	B1	A1	B1	A1	B1
[OII]	3727	7.93 ± 2.78	6.81 ± 4.63	3.38 ± 1.32	1.95 ± 0.68	2.05 ± 0.70	1.56 ± 0.30
		11.64	**7.99**	**3.56**	**1.95**	**2.05**	**1.95**
[NeIII]	3869	1.02 ± 0.56	...	...	0.43 ± 0.31	...	...
		1.42	**...**	**...**	**0.43**	**...**	**...**
Hβ	4861	1.00	1.00	1.00	1.00	1.00	1.00
[OIII]	4959	...	0.95 ± 0.92	...	0.26 ± 0.27	0.80 ± 0.36	0.67 ± 0.23
		...	**0.94**	**...**	**0.26**	**0.80**	**0.66**
[OIII]	5007	2.50 ± 0.95	2.63 ± 1.97	1.71 ± 0.74	2.21 ± 0.84	1.38 ± 0.47	1.62 ± 0.31
		2.39	**2.58**	**1.70**	**2.21**	**1.38**	**1.58**
[OI]	6300	0.47 ± 0.26	...	0.29 ± 0.17	0.21 ± 0.17	0.24 ± 0.18	0.28 ± 0.17
		0.31	**...**	**0.27**	**0.21**	**0.24**	**0.22**
[NII]	6548	2.05 ± 0.84	2.64 ± 1.93	2.30 ± 0.94	1.60 ± 0.59	1.28 ± 0.45	1.74 ± 0.42
		1.30	**2.18**	**2.16**	**1.60**	**1.28**	**1.33**
Hα	6563	4.43 ± 1.46	3.39 ± 2.24	2.98 ± 1.10	2.64 ± 0.87	2.45 ± 0.74	3.66 ± 0.66
		2.80	**2.80**	**2.80**	**2.64**	**2.45**	**2.80**
[NII]	6583	6.06 ± 1.88	5.39 ± 3.50	4.48 ± 1.52	2.92 ± 0.96	2.59 ± 0.78	2.85 ± 0.54
		3.81	**4.44**	**4.21**	**2.92**	**2.59**	**2.18**
[SII]	6716	...	...	...	...	0.82 ± 0.30	0.70 ± 0.16
		...	**...**	**...**	**...**	**0.82**	**0.53**
[SII]	6724	...	1.58 ± 1.26	...	1.73 ± 0.69	1.50 ± 0.57	1.39 ± 0.32
		...	**1.29**	**...**	**1.73**	**1.50**	**1.04**
[SII]	6731	...	...	...	...	0.68 ± 0.27	0.69 ± 0.16
		...	**...**	**...**	**...**	**0.68**	**0.52**
F(Hα)		6.6 ± 0.5	6.6 ± 0.4	4.2 ± 0.5	8.3 ± 0.5	13.7 ± 0.7	19.3 ± 1.2
		16.9	**9.7**	**4.8**	**8.3**	**13.7**	**33.2**
F(Hβ)		1.5 ± 0.4	1.9 ± 1.2	1.4 ± 0.4	3.2 ± 0.9	5.6 ± 1.4	5.3 ± 0.6
		6.0	**3.5**	**1.7**	**3.2**	**5.6**	**11.9**
c		0.60	0.25	0.08	0.00	0.00	0.35
E(B–V)		0.42	0.18	0.06	0.00	0.00	0.25

where R is the projected distance in kpc from the nucleus, Ψ the position angle of the slit and Ψ_0 the position angle of the nodal line ($\Psi_0 = 180°$). The inclination of the galaxy, $i = 49°$, was derived from the isophotal diameter ratio given by DeVaucouleurs et al. (1991), $R_{25} = 1.51$. The fitting was done using the Levenberg-Marquardt method: in order to minimize the uncertainties we had to fix $p = 1$. We then obtained for P.A.=180°: a=-380±50 km s^{-1}, c=3±2 kpc, p=1, $V_{\rm sys} = 6980{\pm}15$ km s^{-1}; the same parameters have been used for the velocity curves measured at the other position angles. At P.A.=200° we see deviations at $\sim -15''$ and around 10″-15″: the former may be related to the presence of a bar along 200°, the latter to the interaction with the companion galaxy H91D. The shape of the rotation curve agrees with that shown by Keel (1996) at P.A. = 220°.

3.3. Hα photometry

Fluxes in the continuum-subtracted Hα image were measured using the POLYPHOT task: HII regions were isolated in the contour map shown in Fig. 2 and inside each aperture fluxes above the background noise level of 10^{-17} erg s^{-1} cm^{-2} pix^{-1} were summed.

To have an estimate of the Hα fluxes, it is necessary to subtract the contribution from [NII] λ6583, which falls in the filter, and correct for internal extinction by dust. From the spectral data we see that [NII]/H$\alpha \sim 0.3 - 0.5$; we adopt the ratio measured in B2$_{270}$, namely the HII region with the highest signal to noise ratio, [NII] λ6583/Hα = 0.3. As concerns internal reddening, from the spectroscopic Hα/Hβ ratios we obtained E(B–V) $\sim 0.3 - 0.9$: the 'true' Hα fluxes may therefore be a factor between 2 and 7 higher than the observed ones. We chose to take as reference the extinction measured in B2$_{270}$, E(B–V) = 0.3: it follows that in some cases the Hα fluxes may have been underestimated.

In order to check the reliability of the whole procedure, we defined a region matching as close as possible the position of the slit in the $B2_{270}$ region. We obtain an undereddened flux $F_{\rm H\alpha} \sim 4.1 \times 10^{-14}$ erg s^{-1} cm^{-2} from the image photometry, whereas $F_{\rm H\alpha} \sim 5.4 \times 10^{-14}$ erg s^{-1} cm^{-2} from the spectroscopic data in Table 5: the difference is in agreement with the uncertainties in the flux calibration of images ($\sim 30\%$) and spectra ($\leq 20\%$) given above.

As concerns the nucleus, the undereddened flux measured in the Hα image is considerably lower, $F_{\rm H\alpha+[NII]} \sim 2 \times 10^{-13}$

Table 5. Emission line ratios in the extranuclear regions. Fluxes are given in units of 10^{-16} erg s^{-1} cm^{-2}.

		P.A. = 180°			P.A. = 200°		P.A. = 270°	
Line	λ	A2	B2	B3	A2	B2	A2	B2
[OII]	3727	0.71 ± 0.05	5.18 ± 1.30	4.04 ± 0.85	2.55 ± 0.43	4.66 ± 0.98	1.69 ± 0.41	0.65 ± 0.04
		1.12	**10.47**	**6.49**	**5.58**	**9.22**	**3.12**	**0.85**
Hδ	4102	...	...	...	...	...	...	0.16 ± 0.02
		...	**...**	**...**	**...**	**...**	**...**	**0.19**
Hγ	4340	...	...	...	...	...	...	0.31 ± 0.02
		...	**...**	**...**	**...**	**...**	**...**	**0.36**
[OIII]	4363	...	...	...	...	...	...	0.01 ± 0.01
		...	**...**	**...**	**...**	**...**	**...**	**0.01**
HeI	4472	...	...	...	...	...	...	0.06 ± 0.01
		...	**...**	**...**	**...**	**...**	**...**	**0.07**
Hβ	4861	1.00	1.00	1.00	1.00	1.00	1.00	1.00
[OIII]	4959	...	...	0.24 ± 0.15	...	0.51 ± 0.33	0.46 ± 0.25	0.05 ± 0.01
		...	**...**	**0.23**	**...**	**0.49**	**0.44**	**0.05**
[OIII]	5007	0.31 ± 0.11	0.85 ± 0.39	0.72 ± 0.27	0.37 ± 0.18	1.21 ± 0.34	0.52 ± 0.23	0.17 ± 0.02
		0.29	**0.78**	**0.68**	**0.34**	**1.12**	**0.48**	**0.16**
HeI	5876	...	...	...	...	...	...	0.09 ± 0.01
		...	**...**	**...**	**...**	**...**	**...**	**0.07**
[OI]	6300	...	0.36 ± 0.16	0.19 ± 0.10	0.23 ± 0.13	0.55 ± 0.24	0.17 ± 0.11	0.04 ± 0.01
		...	**0.17**	**0.12**	**0.10**	**0.27**	**0.09**	**0.03**
[OI]	6364	...	...	...	...	...	...	0.02 ± 0.01
		...	**...**	**...**	**...**	**...**	**...**	**0.01**
[NII]	6548	0.57 ± 0.07	1.26 ± 0.45	0.67 ± 0.15	0.73 ± 0.17	1.07 ± 0.22	0.84 ± 0.21	0.38 ± 0.02
		0.33	**0.55**	**0.38**	**0.29**	**0.48**	**0.41**	**0.27**
Hα	6563	4.83 ± 0.39	6.50 ± 1.50	4.94 ± 0.59	7.14 ± 0.86	6.33 ± 0.95	5.83 ± 0.93	3.88 ± 0.08
		2.80	**2.80**	**2.80**	**2.80**	**2.80**	**2.80**	**2.80**
[NII]	6583	1.91 ± 0.17	4.36 ± 1.09	2.17 ± 0.30	3.32 ± 0.46	3.73 ± 0.60	2.46 ± 0.44	1.23 ± 0.04
		1.10	**1.86**	**1.22**	**1.29**	**1.64**	**1.17**	**0.89**
[SII]	6716	0.77 ± 0.08	...	...	1.83 ± 0.29	2.94 ± 0.56	...	0.41 ± 0.02
		0.43	**...**	**...**	**0.67**	**1.23**	**...**	**0.29**
[SII]	6724	1.37 ± 0.15	3.16 ± 0.92	1.64 ± 0.41	3.08 ± 0.52	5.13 ± 1.03	...	0.70 ± 0.03
		0.76	**1.28**	**0.89**	**1.13**	**2.14**	**...**	**0.49**
[SII]	6731	0.60 ± 0.07	...	...	1.25 ± 0.23	2.19 ± 0.46	...	0.29 ± 0.01
		0.33	**...**	**...**	**0.46**	**0.91**	**...**	**0.20**
F(Hα)		54.6 ± 0.5	22.0 ± 0.7	25.1 ± 0.5	32.4 ± 0.6	26.9 ± 0.3	28.4 ± 0.6	538.8 ± 0.0
		165.1	**121.6**	**79.4**	**216.9**	**141.1**	**126.0**	**1045.0**
F(Hβ)		11.3 ± 0.8	3.4 ± 0.7	5.1 ± 0.5	4.5 ± 0.5	4.3 ± 0.6	4.9 ± 0.7	138.7 ± 2.8
		58.9	**43.4**	**28.4**	**77.5**	**50.4**	**45.0**	**372.6**
c		0.72	1.11	0.75	1.23	1.07	0.96	0.43
E(B–V)		0.50	0.77	0.52	0.86	0.75	0.67	0.30

erg s^{-1} cm^{-2} than that measured in the spectra, $F_{\mathrm{H}\alpha+[\mathrm{NII}]} \sim 5 \times 10^{-13}$ erg s^{-1} cm^{-2}, which is likely due to the fact that the emission in the wings of the broad Hα (FWHM = 70 Å) is missed by the filter (FWHM = 64 Å).

4. Discussion

4.1. Nucleus

In order to have some indication on the physical parameters which may produce the observed nuclear spectrum, we tried to fit the observed line ratios using the Gary Ferland's photoionization code Cloudy 90 (Ferland 1997). The assumed continuum was a power law ($F_\nu \propto \nu^\alpha$) with cutoffs at low ($\lambda = 10\mu$m, $\alpha = 2.5$) and high ($h\nu = 50$keV, $\alpha = -2$) energies. Solar abundances were assumed as a starting point, namely (Grevesse and Anders 1989 and Grevesse and Noels 1993, as given in Ferland 1997):

H: 1.00, He: 1.00×10^{-1}, Li: 2.04×10^{-9}, Be: 2.63×10^{-11}, B: 7.59×10^{-10}, C: 3.55×10^{-4}, N: 9.33×10^{-5}, O: 7.41×10^{-4}, F: 3.02×10^{-8}, Ne: 1.17×10^{-4}, Na: 2.06×10^{-6}, Mg: 3.80×10^{-5}, Al: 2.95×10^{-6}, Si: 3.55×10^{-5}, P: 3.73×10^{-7}, S: 1.62×10^{-5}, Cl: 1.88×10^{-7}, Ar: 3.98×10^{-6}, K: 1.35×10^{-7}, Ca: 2.29×10^{-6}, Sc: 1.58×10^{-9}, Ti: 1.10×10^{-7}, V: 1.05×10^{-8}, Cr: 4.84×10^{-7}, Mn: 3.42×10^{-7}, Fe: 3.24×10^{-5}, Co: 8.32×10^{-8}, Ni: 1.76×10^{-6}, Cu: 1.87×10^{-8}, Zn: 4.52×10^{-8}.

As concerns the NLR, we were not able to fit the observed line ratios with a simple one-component model. As discussed above, the strong [OIII] λ4363 and high ionization lines are likely to be produced in a component with density $\sim 10^7$ cm^{-3}.

Table 6. Emission line ratios computed by Cloudy with different input parameters (see text for details).

Line	λ	A	B	C	D	E	F	G	H	I
		BLR	NLR$_1$	NLR$_2$	NLR	Power law		Thermal		Mixed
[NeV]	3426	0.01	5.20	0.00	3.47	0.00	0.00	0.00	0.00	0.00
[OII]	3727	0.00	0.00	1.25	0.42	5.91	3.55	1.36	1.83	2.64
[NeIII]	3869	0.02	0.45	0.98	0.63	0.54	0.22	0.02	0.05	0.14
H8	3888	0.11	0.12	0.11	0.12	0.11	0.11	0.11	0.11	0.11
[NeIII]	3968	0.01	0.14	0.30	0.19	0.16	0.07	0.01	0.01	0.04
Hϵ	3970	0.15	0.17	0.17	0.17	0.17	0.17	0.17	0.17	0.17
Hδ	4102	0.21	0.27	0.27	0.27	0.27	0.27	0.27	0.27	0.27
Hγ	4340	0.33	0.48	0.48	0.48	0.47	0.47	0.47	0.47	0.48
[OIII]	4363	0.04	0.99	0.06	0.68	0.01	0.00	0.00	0.00	0.00
HeII	4686	0.18	0.70	0.12	0.50	0.09	0.05	0.00	0.00	0.02
Hβ	4861	1.00	1.00	1.00	1.00	1.00	1.00	1.00	1.00	1.00
[OIII]	4959	0.01	0.99	3.26	1.75	0.76	0.05	0.07	0.09	0.27
[OIII]	5007	0.02	2.86	9.42	5.05	2.19	0.15	0.21	0.25	0.77
[FeVII]	5721	0.00	0.29	0.00	0.20	0.00	0.00	0.00	0.00	0.00
HeI	5876	0.20	0.02	0.14	0.06	0.15	0.17	0.12	0.15	0.14
[FeVII]	6087	0.00	0.44	0.00	0.29	0.00	0.00	0.00	0.00	0.00
[OI]	6300	0.01	0.00	0.43	0.14	0.48	0.53	0.02	0.06	0.10
[FeX]	6375	0.01	0.19	0.00	0.13	0.00	0.00	0.00	0.00	0.00
Hα	6563	5.11	2.72	2.86	2.77	2.90	2.92	2.93	2.92	2.91
[NII]	6583	0.00	0.00	3.18	1.07	2.77	2.22	1.00	1.24	1.46
[SII]	6716	0.00	0.00	0.33	0.11	1.22	1.79	0.46	0.67	0.78
[SII]	6724	0.00	0.00	0.98	0.33	2.56	3.11	0.82	1.17	1.37
[SII]	6731	0.00	0.00	0.66	0.22	1.33	1.32	0.35	0.51	0.59

A: Power law, $\alpha = -1.5$, $\log n_{\rm H} = 9.5$, $\log U = -1.5$: best fit for nuclear broad lines
B: Power law, $\alpha = -1.5$, $\log n_{\rm H} = 6.4$, $\log U = -1.5$
C: Power law, $\alpha = -1.5$, $\log n_{\rm H} = 4.5$, $\log U = -3$, N/N$_\odot$ = 2, S/S$_\odot$ = 2
D: Composite model (B+C): best fit for nuclear narrow lines
E: Power law, $\alpha = -1.5$, $\log n_{\rm H} = 3$, $\log U = -3.5$: best fit for the A1 and B1 regions
F: Power law, $\alpha = -1.5$, $\log n_{\rm H} = 2$, $\log U = -4.0$
G: Mihalas, $T_* = 36\,000$ K, $\log n_{\rm H} = 2$, $\log U = -3.2$: best fit for B2$_{270}$
H: Mihalas, $T_* = 38\,000$ K, $\log n_{\rm H} = 2$, $\log U = -3.5$: best fit for A2$_{180}$, B3$_{180}$, A2$_{200}$, A2$_{270}$
I: Mixed model, $\alpha = -1.5$, $\log U = -4.0$ and a Mihalas continuum, $T_* = 38\,000$ K, $\log U = -3.5$, $\log n_{\rm H} = 2$: best fit for B2$_{180}$, B2$_{200}$

Korista and Ferland (1989) suggested that high-ionization lines may be produced in low density gas, $\log U = 0, n_{\rm H} = 10$ cm^{-3}; however, the intensities predicted by such models for [FeVII] λ6087 are too low to account for the observed values. The observed [FeVII] λ3759/[FeVII] λ6087 is $\sim$ 0.7-1.0: from Fig. 2 in Nussbaumer and Storey (1982) we obtain $T_{\rm e} \leq 20\,000$ K. If we assume $T_{\rm e} = 15\,000$ K, a density $n_{\rm e} \sim 10^8$ cm^{-3} is inferred. The observed [FeVII] λ5721/[FeVII] λ6087 ~ 0.7 is in good agreement with the theoretical value 0.66 from Nussbaumer and Storey.

In order to simplify the choice of the model input parameters, we considered a two-component model and made the following assumptions:

1. The main contribution to [OIII] λ4363 and other lines of high critical density such as [FeVII] λ6087 and [FeX] λ6375 comes from high density clouds ($n_{\rm H} > 10^6$ cm^{-3}).
2. Other lines such as [OIII] λ5007, [NII] λ6583, [OI] λ6300 and [SII] $\lambda\lambda$6716, 6731 are mainly produced in low density clouds ($n_{\rm H} < 10^5$ cm^{-3}).
3. As concerns the Balmer lines, both components contribute in an unknown amount to the overall emission.

Given these assumptions, we adopted the following procedure. We started from the high density component. In this case, the observed ratio to Hβ, $R_{\rm obs}$, is:

$$R_{\rm obs} \sim \frac{F_{\rm HD}(\lambda)}{F_{\rm HD}(H\beta) + F_{\rm LD}(H\beta)} = \frac{R_{\rm HD}}{1+\chi^{-1}}, \tag{2}$$

where $F_{\rm LD}(\lambda)$ and $F_{\rm HD}(\lambda)$ are the line fluxes computed in the low and high density models respectively, $R_{\rm HD}$ is the ratio that would be obtained considering the high density component alone and $\chi = F_{\rm HD}(H\beta)/F_{\rm LD}(H\beta)$. We looked for the model parameters (ionization parameter, hydrogen density, thickness of the cloud and chemical abundance) giving as large as possible [OIII] λ4363/Hβ and [FeVII] λ6087/Hβ ratios (namely above the observed values of ~ 0.6 and ~ 0.5 respectively) and then computed χ from Eq. 2.

Starting from this value of χ, we obtained the line ratios in the low-density component, $R_{\rm LD}$, assuming that for these lines:

$$R_{\rm obs} \sim \frac{F_{\rm LD}(\lambda)}{F_{\rm HD}(H\beta)+F_{\rm LD}(H\beta)} = \frac{R_{\rm LD}}{1+\chi}. \quad (3)$$

Finally, line ratios from both components were computed as:

$$R_{\rm HD+LD} = \frac{F_{\rm HD}(\lambda)+F_{\rm LD}(\lambda)}{F_{\rm HD}(H\beta)+F_{\rm LD}(H\beta)}, \quad (4)$$

where the fluxes given as output from the low and high density models were rescaled so that $F_{\rm HD}(H\beta)/F_{\rm LD}(H\beta) = \chi$. These values were compared with the observed ones and the whole procedure was repeated with different values of χ and different model parameters, until a satisfactory fit was achieved.

The best fit for the high density component was obtained, see col. B in Table 6, with $\alpha = -1.5$, $n_{\rm H} = 10^{6.4}$ cm^{-3}, $\log U = -1.5$, $\Delta R = 10^{14}$ cm. From Eq. 2 we obtained $\chi \sim 2$. As concerns the low density component, the parameters giving the best fit were $\alpha = -1.5$, $n_{\rm H} = 10^{4.5}$ cm^{-3}, $\log U = -3$, $\Delta R = 10^{16}$ cm and a nitrogen and sulphur overabundance: N/N$_\odot$=2, S/S$_\odot$=2; the results are given in Table 6, col. C.

Line ratios obtained from the sum of the two components are given in col. D of Table 6. The whole emission line spectrum (broad, semi-broad and narrow components) is graphically shown in Fig. 12b. Even if we followed a simple approach, the results are quite satisfactory. The fact that most of the flux of the Balmer lines should be produced by the high density clouds, seems in agreement with the fact that Balmer lines are wider than the forbidden ones which are predicted to be produced in the lower density component. Spectra with higher resolution would be required in order to look for the presence of more components in the line profiles.

In the BLR, we have too few broad lines to constrain the parameters of a model. Typical parameters for the BLR are: $\alpha = -1.5$, $n_{\rm H} = 10^{9.5}$ cm^{-3}, $\log U = -1.5$, $\Delta R = 10^{13}$ cm. The line ratios produced by this model are given in Table 6, col. A.

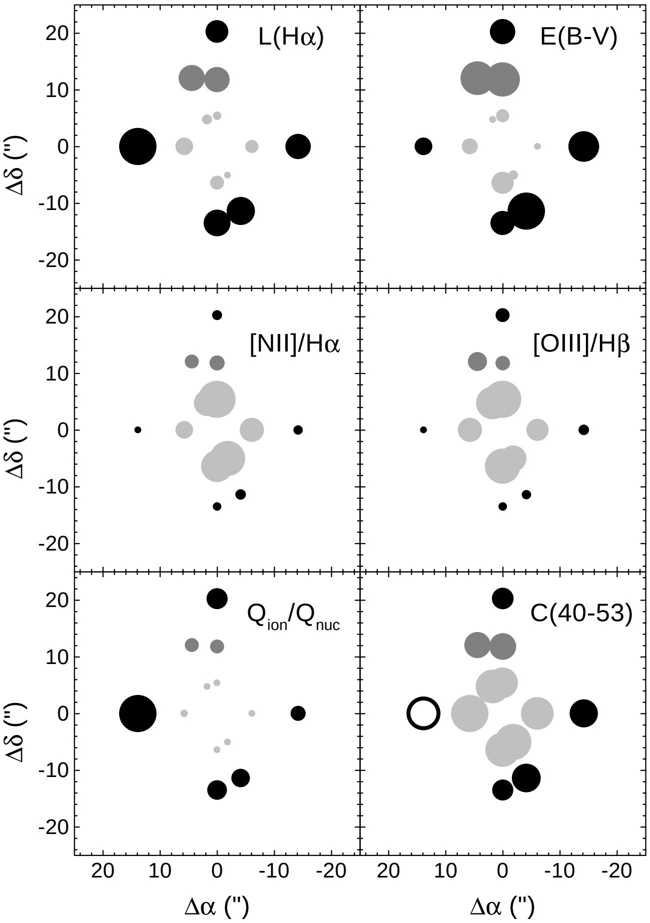

Fig. 13. The panels show the following quantities determined from spectroscopic data in the circumnuclear and extranuclear regions: dereddened Hα luminosities (L(Hα)), reddening (E(B–V)), line ratios ([NII] λ6583/Hα, [OIII] λ5007/Hβ), local to nuclear ionizing photon ratio ($Q_{\rm ion}/Q_{\rm nuc} = \eta^{-1}$) and continuum color index (C(40-53)). The size of each circle is proportional to the measured value; the color indicates the ionization source as deduced from line ratios (light gray: non-thermal ionization; dark gray: mixed ionization; black: thermal ionization). The open circle in the C(40-53) panel indicates the negative value of the index in the B2$_{270}$ region.

4.2. Circumnuclear and extranuclear regions

In order to check whether ionization in the extranuclear regions A2, B2, B3 is given in part by the non-thermal nuclear continuum, we compared the rate (photons s^{-1}) of ionizing photons emitted from the nucleus reaching each region in absence of absorption ($Q_{\rm nuc}$) with the rate of ‘local’ ionizing photons computed from the observed, extinction corrected Hα luminosities ($Q_{\rm ion}$), namely (Osterbrock 1989):

$$\begin{aligned} Q_{\rm nuc} &= Q_{\rm NLR}\frac{\Omega}{4\pi}, \quad (5)\\ Q_{\rm ion} &= 7.3\times10^{51}\left(\frac{L_{\rm H\alpha}}{10^{40}{\rm erg\,s^{-1}}}\right), \end{aligned}$$

where Ω is the solid angle of each region seen from the nucleus, $\Omega/4\pi$ its covering factor, $Q_{\rm NLR}$ is the number of ionizing photons required to produce the narrow Hα luminosities: the values observed along the three position angles were averaged together, giving $Q_{\rm NLR} = 4\pm1\times10^{52}$ photons s^{-1}. We then computed the quantity $\eta = Q_{\rm nuc}/Q_{\rm ion}$, that is the ratio between nuclear and ‘local’ ionizing photons. As we can see in Table 7, the results are in good agreement with what was found from the analysis of the VO diagrams. The inner A1 and B1 are most likely to be ionized by the nucleus ($\eta \geq 30\%$); in the outer regions η varies between 1% and 5% (see Table 7 and Fig. 13), with the highest values in the B2 regions at P.A.=180° and 200°.

According to Storchi-Bergmann et al. (1995), there should be a sequence from starbursts to Seyfert galaxies in the continuum color index C(40-53), defined as:

$$C\,(40-53) = -2.5\log\frac{F_{\lambda4020}}{F_{\lambda5313}}, \quad (6)$$

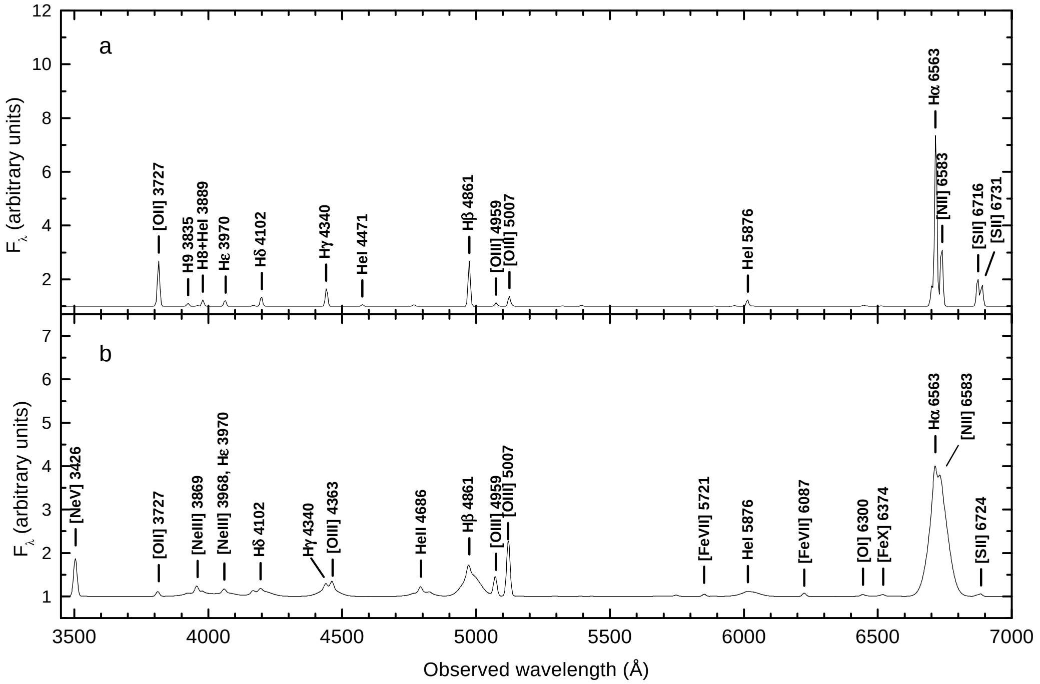

Fig. 12. Synthetic spectra for the extranuclear region $\mathrm{B2}_{270}$ (a) and the nucleus (b). The parameters of the models are those discussed in the text, a reddening E(B–V) = 0.3 has been applied to the model of B2 in order to match the observed spectrum.

Table 7. Physical properties in the extranuclear regions. ψ and ψ_a are given in $M_\odot$ yr^{-1} and $M_\odot$ yr^{-1} pc^{-2} respectively.

	P.A. = 180°					P.A. = 200°				P.A. = 270°			
	A1	B1	A2	B2	B3	A1	B1	A2	B2	A1	B1	A2	B2
$\log L_{\mathrm{H}\alpha}$	39.23	38.82	40.22	40.09	39.90	38.69	38.93	40.34	40.15	39.14	39.53	40.11	41.02
η (%)	77	185	2	5	2	252	138	3	5	93	38	4	1
$\log Q_\mathrm{ion}$	51.10	50.69	52.09	51.95	51.77	50.55	50.79	52.20	52.02	51.01	51.39	51.97	52.89
$\mathcal{N}$(O5)	–	–	243	179	117	–	–	320	208	–	–	186	1537
ψ	–	–	0.118	0.087	0.057	–	–	0.155	0.101	–	–	0.090	0.746
$\log \psi_\mathrm{a}$	–	–	-7.44	-7.60	-7.75	–	–	-7.38	-7.68	–	–	-7.68	-6.79
C(40–53)	0.50	0.37	0.02	0.23	0.04	0.58	0.46	0.32	0.21	0.45	0.60	0.28	-0.46

where the fluxes are averaged on 15Å bins centered on the given wavelengths In their sample of galaxies Storchi-Bergmann et al. (1995) find that C(40-53) = -0.36 ± 0.16 in HII galaxies, -0.15 ± 0.10 in starburst galaxies, 0.14 ± 0.20 in Seyferts with evidence of circumnuclear star formation and 0.34 ± 0.16 in 'pure' Seyferts. We computed C(40-53) for all the circumnuclear regions; the results are shown in Table 7 and Fig. 13. It is interesting to note that we find the 'reddest' colors in the inner regions A1 and B1, C(40-53) ≥ 0.4, the 'bluest' colors in A2 and B3 (P.A.=180°) and B2 (P.A.=270°), C(40-53) ≤ 0; in the other regions we have 'intermediate' colors, C(40-53) $\sim 0.2 - 0.3$. Even if we are aware that C(40-53) may be affected by internal dust reddening, this trend is in agreement with an increasing star formation at increasing distances from the nucleus.

We shall now assume that photoionization alone produces the observed line intensities, in order to isolate those HII regions which may be safely considered as unaffected by the nonthermal source: for these regions we shall compute the star formation rates per projected unit area and compare them with the values observed in the HII regions of non active spiral galaxies. If photoionization alone is considered, three situations may occur:

1. Photoionization by the AGN power-law (A1 and B1 regions).
2. Photoionization by stars ($\mathrm{A2}_{180}$, $\mathrm{B3}_{180}$, $\mathrm{A2}_{200}$, $\mathrm{A2}_{270}$, $\mathrm{B2}_{270}$).
3. Photoionization by both the above components ($\mathrm{B2}_{180}$, $\mathrm{B2}_{200}$): the cloud is an HII region which is also ionized by the photons emitted by the AGN.

In the first case (photoionization by the AGN), the best fit is obtained (see Figs. 6, 7, 8 and Table 6 col.E) with the following parameters: solar abundances, $\alpha = -1.5$, $\log n_\mathrm{H} = 3$, $\log U = -3.5$.

In the second case (photoionization by stars), we adopted a density $\log n_\mathrm{H} = 2$, as suggested by the intensity ratio of the [SII] lines, and a non-LTE Mihalas (1972) stellar continuum ($\log g = 4$); we did not try to change the chemical abundance from the solar value. The best fit for line ratios in $\mathrm{B2}_{270}$ is given by $T_* = 36\,000$ K, $\log U = -3.2$, see col.G in Table 6. In the other regions, a higher stellar temperature is required,

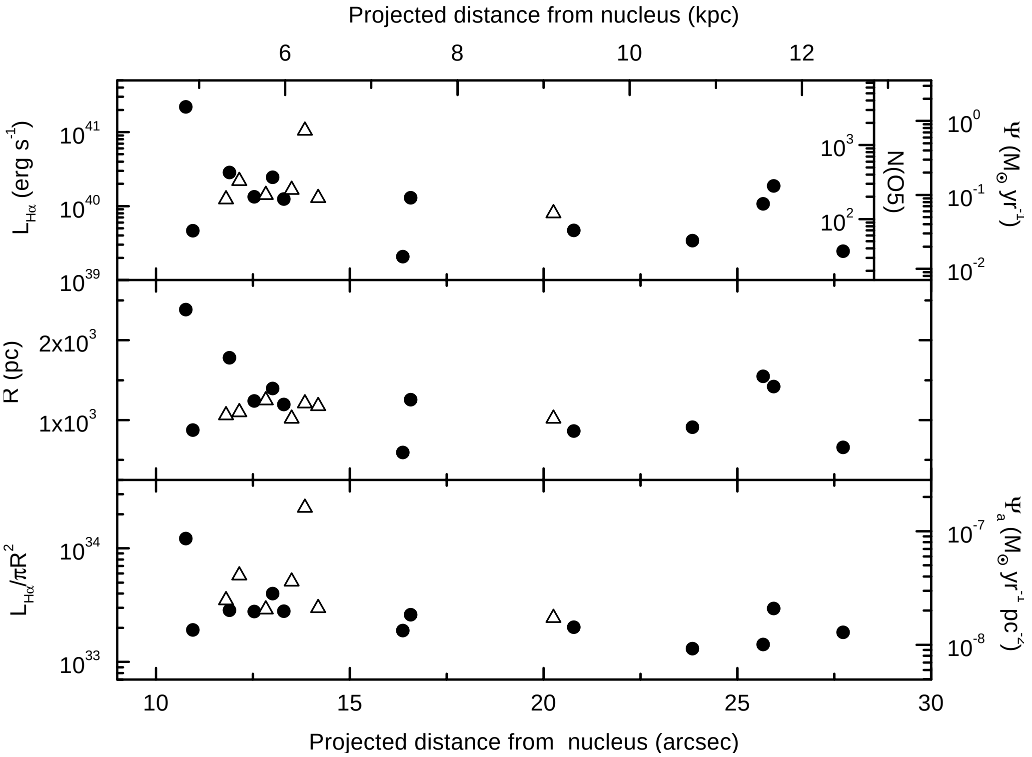

Fig. 14. Hα luminosities and star formation rates in the circumnuclear HII regions derived from spectroscopic (triangles) and imaging (circles) data. *Up*: Hα luminosities, corrected for internal reddening as explained in the text and equivalent number of O5 ionizing stars (inner right axis). *Middle*: sizes defined as the radius of the circularized area, $R = (A/\pi)^{0.5}$. *Bottom*: Hα luminosities per unit area. The conversion to star formation rates is shown in the right axis.

$T_* \sim 38\,000$ K, the ionization parameter is in the range $\log U = -3, -3.5$ (col.H in Table 6).

In order to handle the third situation, we fixed the input parameters of the thermal component to those found in 'simple' HII regions, $T_* = 38\,000$ K, $\log U_{\rm th} = -3.5$, $\log n_{\rm H} = 2$. We added to this continuum the power law component, $\alpha = -1.5$ and computed a grid with different values of the ionization parameter for this component, $U_{\rm pl}$. For $\log U_{\rm pl} > -3$ the ionization of the cloud is dominated by the power law component and line ratios are those given by single component AGN models. If $\log U_{\rm pl} \le -3.5$, however, the thermal contribution becomes important and line ratios migrate toward the HII values. We find that the intermediate line ratios measured in B2$_{180}$ and B2$_{200}$ are in good agreement with such a model assuming $\log U_{\rm pl} = -4$. The model line ratios are shown in col.I of Table 6; we also show for comparison in col.F the line ratios produced by the power law component alone.

From the number of ionizing photons required to produce the observed Hα luminosities we estimated (Table 7) the equivalent stellar content in terms of O5 stars ($\mathcal{N}$(O5)), assuming that each O star produces $\sim 5 \times 10^{49}$ ionizing photons s^{-1} (Osterbrock 1989). Star formation rates (ψ) for stars of mass 0.1 to 100 $M_\odot$ have been computed from the reddening corrected Hα luminosities using the formula given by Hunter and Gallagher (1986):

$$\psi({\rm H}\alpha) = 7.07 \times 10^{-42} L({\rm H}\alpha) \quad M_\odot {\rm yr}^{-1}. \tag{7}$$

The same quantities have been then computed from the Hα luminosities measured in the narrow band filter image; all values are shown in Fig. 14. The equivalent stellar content is in the range from ~ 30 to ~ 500 with the exception of the region B2 at P.A.=270° where $\mathcal{N}$(O5) $\sim$ 1500 in the region covered by the slit, ~ 3000 in the whole HII region: this is a value typical of a supergiant HII region (Kennicutt, Edgar and Hodge 1989).

The star formation rates *per unit area* measured in the Hα image are comparable with those given by Kennicutt (1988) for the brightest HII regions in a sample of 95 normal spiral galaxies: in this sample the star formation rates are well fitted by a gaussian distribution around a mean value $\log \psi_a({\rm H}\alpha) \sim -7.2 \pm 0.3\ M_\odot$ yr^{-1} pc^{-2}. We find that in the brightest HII region in NGC 7214, namely the one identified as B2$_{270}$ in the long slit spectra, $\log \psi_a({\rm H}\alpha) \sim -7.1$, whereas in the other regions $\log \psi_a({\rm H}\alpha)$ is between -8.0 and -7.4. We show also for comparison in Fig. 14 the star formation rates per unit area computed from the spectroscopic data, although these values are not so reliable since in most cases only small parts of the HII regions are covered by the slit.

The spectroscopically measured Hα luminosity from the nucleus is $\sim 4.5 \times 10^{41}$ erg s^{-1}, whereas the total Hα luminosity from circumnuclear regions measured from Hα imaging is $\sim 3.5 \times 10^{41}$ erg s^{-1} or higher depending on the amount of dust, as we adopted a lower limit E(B–V) = 0.3. It is therefore very likely that in the case of NGC 7214 extended far infrared emission due to circumnuclear star formation is present and that it may at least in part explain the steep $\alpha(60, 25)$ index.

5. Conclusions

In this paper we analyzed the spectroscopic and narrow-band Hα photometric properties of the nuclear and circumnuclear regions of NGC 7214; in particular, the photoionization code CLOUDY 90 was used to find the model parameters which best

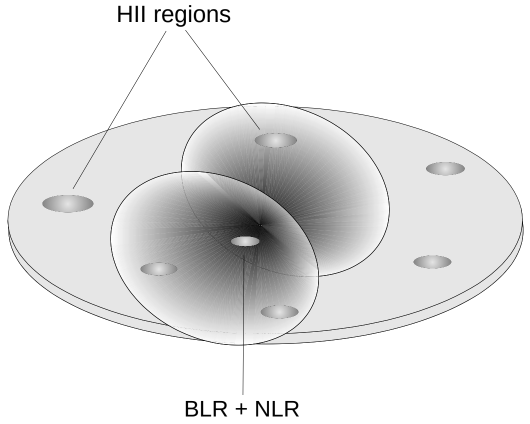

Fig. 15. A possible sketch of the situation in NGC 7214: at increasing distances from the nucleus we have an increase in the probability to observe HII regions which lie outside the ionizing beam

fit the observed line ratios in both nuclear and circumnuclear regions.

In the nucleus, we found that the observed line intensities require, in addition to the very high density ($\log n_{\rm H} \sim 9.5$) clouds in the Broad Line Region, at least two populations of clouds in the Narrow Line Region, namely: (1) thin ($\Delta R \sim 10^{14}$ cm) dense ($\log n_{\rm H} \sim 6.4$) clouds producing [OIII] λ4363 and high-ionization lines ([FeVII] and [FeX]); (2) thicker ($\Delta R \sim 10^{16}$ cm), less dense ($\log n_{\rm H} \sim 4.5$) clouds producing other lines of lower ionization.

In the circumnuclear regions, we tried to determine whether the gas where emission lines are produced is most likely to be ionized by the AGN, or there is evidence of star formation in the circumnuclear environment. We did not find any evidence about the existence of starburst regions in the inner ($\sim$ 1 kpc) regions of the galaxy: the main contribution to the ionization of the gas up to $\sim$ 2 kpc appears to be the non thermal continuum produced by the AGN. At higher distances, however, we observe a more complex situation, where both HII regions and regions which are at least partially ionized by the AGN coexist.

In the framework of the unified model (Antonucci 1993), we observe a Seyfert 1 galaxy when our line of sight lies from within 31° of the torus polar axis; otherwise, a Seyfert 2 is observed. We suggest (Fig. 15) that in the case of NGC 7214 the nucleus is surrounded by HII regions with weak or moderate star formation. At low projected distances ($\sim$ 2 kpc) from the nucleus we mainly observe regions which are illuminated by the beam and whose ionization is AGN like. At higher projected distances (~ 5 kpc), we observe both regions which are inside the beam and regions which are outside it: in the former case we have a 'pure' HII region; in the latter case, given the dilution of the beam fluxes and the low luminosity of the HII region, the ionization of the gas is determined by the contribution of both components.

From the inferred star formation rates it appears that we see normal disk HII regions without any enhancement in the star formation activity; such an enhancement is only detected in the region $\mathrm{B2}_{270}$. The HII regions are distributed in a ring around the nucleus and this, together with the highly distorted morphology of the galaxy, suggests that star formation is related to the ongoing interaction with the companion galaxy.

Acknowledgements. This research has made use of the NASA-IPAC extragalactic database (NED) which is operated by the Jet Propulsion Laboratory, Caltech, under contract with the National Aeronautics and Space Administration. We are grateful to G. Ferland for having made available to the scientific community his photoionization code Cloudy. We wish to thank the referee, dr. L. C. Ho, for his comments which improved the paper.

References

Antonucci, R.R.J. 1993, ARA&A, 31, 473
Barnes, J.E., and Hernquist, L. 1992, ARA&A, 30, 705
Bertola, F., Bettoni, D., Danzinger, J., Sadler, E., Sparke, L., and Zeeuw, T. 1991, ApJ, 373, 369
Burstein, D., and Heiles, C. 1984, ApJS, 54, 33
Cohen, R.D. 1983, ApJ, 273, 489
Dahari, O. 1985, ApJS, 57, 643
De Robertis, M.M., and Osterbrock, D.E. 1984, ApJ, 286, 171
de Vaucouleurs, G., de Vaucouleurs, A., Corwin, H.G., Buta, R.J., Paturel, G., and Fouque, P. 1991, Third Reference Catalogue of Bright Galaxies (ed. Springer Verlag)
Ferguson, J.W., Korista, K.T., and Ferland, G.J. 1997, ApJS, 110, 287
Ferland, G.J. 1997, Hazy: a brief introduction to Cloudy, University of Kentucky, Department of Physics and Astronomy Internal Report
Grevesse, N., and Anders, E. 1989, in AIP Conf. Proc. 183, Cosmic Abundances of Matter, ed. C.J. Waddington (New York: AIP), 1
Grevesse, N., and Noels, A. 1993, in Origin and Evolution of the Elements, ed. N. Prantzos, E. Vangioni-Flam, and M. Casse (Cambridge: Cambridge Univ. Press), 15
Hernquist, L., and Mihos, J.C. 1995, ApJ, 448, 41
Hickson, P. 1982, ApJ, 255, 382
Ho, L.C., Filippenko, A.V., and Sargent, W.L.W. 1993, ApJ, 417, 63
Hunter, D.A., and Gallagher, J.S. 1986, PASP, 98, 5
Joly, M. 1988, A&A, 192, 87
Keel, W.C. 1996, AJ, 111, 696
Kennicutt, R.C. 1988, ApJ, 334, 144
Kennicutt, R.C., Edgar, B.K., and Hodge, P.W. 1989, ApJ, 337, 761
Korista, K.T., and Ferland, G.J. 1989, ApJ, 343, 678
Lonsdale, C.J. 1989, Catalogued galaxies and quasars observed in the IRAS survey Vers. 2, Jet Propulsion Laboratory
Mihalas, D. 1972, Non-LTE Model Atmospheres for B and O Stars (Boulder: NCAR) (NCAR-TN/STR-76)
Miller, J.S., and Mathews, W.G. 1972, ApJ, 172, 593
Moorwood, A.F. 1996, SSR, 77, 303
Mulchaey, J.S., Koratkar, A., Ward, M.J., Wilson, A.S., Whittle, M., Antonucci, R.J.J., Kinney, A.L., and Hurt, T. 1994, ApJ, 436, 586
Nussbaumer, H., and Storey, P.J. 1982, A&A, 113, 21
Osterbrock, D.E., and Koski, A.T. 1976, MNRAS, 176, 61P
Osterbrock, D.E. 1981, ApJ, 246, 696
Osterbrock, D.E., 1989, in Astrophysics of Gaseous Nebulae and Active Galactic Nuclei (Mill Valley: University Science Books)
Radovich, M., and Rafanelli, P. 1996, A&A, 306, 97
Rafanelli, P., Violato, M., and Baruffolo, A., 1995, AJ, 109, 1546
Storchi-Bergmann, Th., Kinney, A.L., and Challis, P. 1995, ApJS, 98, 103
Veilleux, S., and Osterbrock, D.E. 1987, ApJS, 63, 295, VO
Whitford, A.E. 1958, AJ, 63, 201
Winkler, H. 1992, MNRAS, 257, 677